IOWA STATE UNIVERSITY
Digital Repository

Mechanical Engineering Publications | Mechanical Engineering

7-8-2021

Global Gas-Phase Oxidation Rates of Select Products from the Fast Pyrolysis of Lignocellulose

Chad Peterson
Iowa State University

Robert C. Brown
Iowa State University, rcbrown3@iastate.edu

Follow this and additional works at: https://lib.dr.iastate.edu/me_pubs

 Part of the Catalysis and Reaction Engineering Commons, and the Energy Systems Commons

The complete bibliographic information for this item can be found at https://lib.dr.iastate.edu/me_pubs/490. For information on how to cite this item, please visit http://lib.dr.iastate.edu/howtocite.html.

This Article is brought to you for free and open access by the Mechanical Engineering at Iowa State University Digital Repository. It has been accepted for inclusion in Mechanical Engineering Publications by an authorized administrator of Iowa State University Digital Repository. For more information, please contact digirep@iastate.edu.

Global Gas-Phase Oxidation Rates of Select Products from the Fast Pyrolysis of Lignocellulose

Abstract

The oxidation kinetics for products of fast pyrolysis at low temperatures (<600 >°C) are not well-known. These will be important in an effort to model autothermal pyrolysis, which has been recently developed to intensify the process but which occurs at much lower temperatures than combustion. This study determines global oxidation rates at 400–600 °C for three important products of fast pyrolysis: levoglucosan, xylose, and acetic acid. Experiments were performed in a fluidized bed pyrolyzer with the reactor modeled as a series of continuously stirred reactors and plug flow reactors to determine reaction rates. Oxidation rates at 500 °C for the three model compounds varied by a factor of 10.

Keywords

Organic reactions, Oxygen, Oxidation, Pyrolysis, Kinetics

Disciplines

Catalysis and Reaction Engineering | Energy Systems | Mechanical Engineering

Comments

This document is the unedited Author's version of a Submitted Work that was subsequently accepted for publication in *Energy & Fuels*, copyright © American Chemical Society after peer review. To access the final edited and published work see DOI: 10.1021/acs.energyfuels.1c01207. Posted with permission.

This article is available at Iowa State University Digital Repository: https://lib.dr.iastate.edu/me_pubs/490

Global Gas-Phase Oxidation Rates of Select Products from the Fast Pyrolysis of Lignocellulose

Chad A. Peterson[1], Robert C. Brown[1,2]

[1]*Department of Mechanical Engineering, Iowa State University, Ames, IA 50011, United States*

[2]*Bioeconomy Institute, Iowa State University, Ames, IA 50011, United States*

Corresponding author's e-mail address: rcbrown3@iastate.edu

Abstract

The oxidation kinetics for products of fast pyrolysis at low temperatures (<600°C) are not well known. These will be important in effort to model autothermal pyrolysis, which has been recently developed to intensify the process, but which occurs at much lower temperatures than combustion. This study determines global oxidation rates at 400-600°C for three important products of fast pyrolysis: levoglucosan, xylose, and acetic acid. Experiments were performed in a fluidized bed pyrolyzer with the reactor modeled as a series of CSTRs and PFRs to determine reaction rates. Oxidation rates at 500°C for the three model compounds varied by a factor of ten.

Keywords:

Pyrolysis; autothermal pyrolysis; oxidation; global rates; levoglucosan; xylose; acetic acid

1. Introduction

Fast pyrolysis is an endothermic process with energy conventionally provided through heat transfer into the reactor.[1] This thermal energy is conventionally provided by either indirect contact or direct contact heat transfer. As a reactor scales in size, its surface area-to-volume ratio decreases, eventually resulting in heat transfer becoming rate limiting to the process.[2] As an alternative, Polin et al.[3] recently demonstrated that addition of a small amount of oxygen into the pyrolyzer can provide the enthalpy for pyrolysis by partially oxidizing products of pyrolysis. As

little as one-tenth of the oxygen required for complete oxidation can sustain this autothermal (partial oxidative) process. By generating energy internally, heat transfer is eliminated, simplifying reactor design.

Given the value of the heavier molecular weight components of bio-oil (sugars and phenolic compounds), autothermal pyrolysis should be contrived to selectively oxidize other pyrolysis products such as biochar and low molecular weight compounds. Fortuitously, biochar appears to be preferentially oxidized in comparison to vapor products although small losses in condensable products are observed.[3,4] A better understanding of the rates of partial oxidation of pyrolysis products would advance the design of autothermal pyrolyzers. Kinetic data is well known for oxidation of gaseous fuels at elevated (combustion) temperatures (>1000°C).[5,6] However, kinetic data appropriate to oxidation at pyrolysis temperatures (<600°C) is largely unavailable in the scientific literature. Progress in autothermal pyrolysis will require a better understanding of the oxidation reactions that drive the process and affect product composition and distribution. Towards this goal, we have recently reported reaction rates on "reduced temperature" oxidation of biochar.[7]

Secondary pyrolysis reactions that decompose vapors in the absence of oxygen have been well studied, although reported rates in the literature vary greatly.[8–12] Fukutome et al. [8] determined that gas phase decomposition of levoglucosan follow first order kinetics distinguished by two distinct temperature regimes. Shin et al. [9] studied the decomposition of various carbohydrate-derived products, including levoglucosan, again finding first order kinetics accurately described the decomposition rate. However, despite similarities in experimental methods employed by these two research groups, their results varied by up to an order of magnitude (Table 1).

Fukutome et al.[8] suggested this difference may have been caused by mass transfer limitations arising from molten levoglucosan in the work of Shin et al.[9]

Table 1. Calculated kinetic rate coefficient of levoglucosan decomposition. Below 600°C there is an order of magnitude difference in the decomposition rate. Note: Fukutome has a low temperature regime (550-600°C) and elevated temperature (>600°C) regime.

	Kinetic Rate Coefficient (s^{-1})			
Source	**550°C**	**600°C**	**650°C**	**700°C**
Fukutome et al. [8]	0.956	3.271	5.335	8.520
Shin et al. [9]	0.059	0.280	1.116	3.865

Given the prominence of levoglucosan among the products of fast pyrolysis[13], the global rate of pyrolysis vapor decomposition is expected to be similar to that for levoglucosan. Liden et al.[10] measured the rate of secondary vapor decomposition of tar (bio-oil) using a fluidized bed reactor at a temperature range of 400-600°C by varying gas residence time. Similar work by Morf et al.[11] pyrolyzed fir and spruce wood chips in a fixed bed followed by a heated tubular reactor where secondary gas phase decomposition occurred. Baumlin et al.[12] similarly used a heated tubular reactor to measure the homogeneous decomposition of bio-oil vapors into non-condensable gases. The studies of Liden et al.[10], Morf et al.[11], and Baumlin et al.[12] yielded similar global decomposition rate coefficients of bio-oil vapors (Table 2).

Table 2. Decomposition kinetic rate coefficient calculated for bio-oil vapors. Reaction rates were determined to follow first order kinetics.

	Kinetic Rate Coefficient (s^{-1})		
Source	**500°C**	**600°C**	**700°C**
Liden et al. [10]	0.233	1.582	7.248
Morf et al. [11]	0.267	1.044	3.088
Baumlin et al. [12]	0.199	0.569	1.312

The average of the three rates at 500°C (0.271 s^{-1}) is nearly identical to the decomposition rate of levoglucosan extrapolated from Fukutome et al.[8] at 500°C (0.238 s^{-1}). The comparable rates

between these overall decomposition models and the levoglucosan experiments of Fukutome et al.[8] provide additional evidence that the work of Shin et al.[9] was experimentally biased.

Comprehensive reaction mechanisms that include decomposition and oxidation reactions of pyrolytic vapors have been developed over several decades.[14] Recently, Debiagi et al.[15] updated the mechanism predicting a rate of levoglucosan decomposition that was comparable to experimental observations.[9] The mechanism of Debiagi et al.[15] was updated and incorporated into the comprehensive combustion mechanism of Ranzi et al.[16] This mechanism contains thousands of elementary reactions and hundreds of intermediate species relevant to high temperature decomposition and oxidation of products from biomass pyrolysis. Despite these significant efforts in developing reaction mechanisms, shortcomings remain. In particular, the Ranzi mechanism used Shin et al.'s[9] levoglucosan decomposition rate for model validation, which as previously described, appears to be flawed. Another shortcoming of the Ranzi mechanism is that it was originally developed for hydrocarbon oxidation and subsequently expanded to include oxygenated compounds.[14,17,18] This updated mechanism has received minimal validation at conditions relevant to the relatively low temperature operating conditions of autothermal pyrolysis of biomass.

Dhahak et al.[19] employed the Ranzi mechanism in combination with several other mechanisms to achieve an updated model with improved decomposition rates for several pyrolysis products (including levoglucosan, anisole, and hydroxyacetaldehyde) derived from credible experimental data. This model accurately described the oxidation of many hydrocarbon products as well as guiacol, a lignin pyrolysis product. While the model is reported to be an improvement over earlier reaction mechanisms, oxidation kinetics relevant to the products of biomass pyrolysis,

such as levoglucosan and xylose, were not included. Likewise, the model employed Shin's discredited levoglucosan decomposition rate.[9]

Combustion of solid fuels is often described by global oxidation models rather than attempting to build reaction networks of elementary reactions. These models include devolatilization (pyrolysis), char oxidation, and tar (condensable vapors) oxidation steps.[20,21] Condensable vapors are grouped together and approximated as a single chemical entity with an elemental composition of $CH_{1.65}O_{0.91}$ for coal-derived tar and $CH_{0.99}O_{0.88}$ for biomass-derived tar [3]. The global tar oxidation rate is a modified Arrhenius equation from Smoot and Smith [22]:

$$\mathbf{rate} = \mathbf{A T^{0.3} e^{-\frac{E_a}{RT}} C_{O_2} C_{CHO}^{0.5}} \quad (1)$$

where A is the pre-exponential factor (20,700 s^{-1}), E_a the activation energy (80.2 kJ mol^{-1}), T the gas temperature (K), and R the universal gas constant (0.008314 kJ mol^{-1} K^{-1}). The reaction is first order for oxygen and 0.5 for fuel.

Dryer and Westbrook[23] developed a one-step hydrocarbon combustion model that was subsequently adapted to ethanol oxidation.[24] The rate expression is a conventional Arrhenius equation:

$$\mathbf{rate} = \mathbf{A e^{-\frac{E_a}{RT}} C_F^{0.15} C_{O_2}^{1.6}} \quad (2)$$

where A is equal to 1.55×10^{10} s^{-1} and E_a is 125.6 kJ mol^{-1}. The reaction order is 1.6 for oxygen and 0.15 for fuel. Despite similar global models, the rate coefficients differ by orders of magnitude at pyrolysis temperatures. The objective of the present study was to reduce the uncertainty in the decomposition and oxidation kinetics of select compounds relevant to

autothermal pyrolysis. Three model compounds representative of biomass pyrolysis products were investigated: xylose, acetic acid, and levoglucosan. Global oxidation rates were determined at temperatures less than 600°C and the Arrhenius parameters calculated. Additional experiments were conducted on the gas phase degradation of levoglucosan to validate the hydrodynamic model.

2. Methods

2.1. Continuous reactor system

Experiments were performed in a bubbling fluid bed reactor system illustrated in Figure 1. The reactor was constructed from 316 stainless steel pipe of 3.81 cm diameter and 42 cm length. Bed material was 400 grams of 500-600 μm diameter sand for oxidation experiments and 250-300 μm diameter sand for levoglucosan decomposition experiments. Gas flow controllers allowed mixing of air and nitrogen gas to produce oxygen concentrations up to 21 vol%. These two controllers allowed for identical flow conditions (i.e., fluidization gas) for model compounds with different stoichiometric requirements. For all the combustion experiments, the equivalence ratio was ~1.05 or slight excess of oxygen needed for complete oxidation. A peristaltic pump continuously fed the aqueous solution of reactant at concentrations described below at rates of 2-5 ml min^{-1}. Instantaneous mass flow measurements were attained by placing the liquid supply cannister atop an analytical balance. The reactor had a small stainless-steel tube inserted 5 cm above the plenum, allowing the injection of the reactant solution into the reactor. A heat-traced stainless steel line conveyed pyrolysis product to a gas cyclone that removed elutriated sand. The fluidized bed reactor, transfer line, and cyclone were heat traced to the same temperature as the reactor (435-550°C) to prevent condensation of product. After the transfer line, an Exergy™ shell and multi-tube condenser (operated at 10°C) collected the condensate in a 250mL bottle.

Gas temperature at the condenser outlet was <10°C. Following the condenser, a glass wool packed bed collected any aerosols to prevent their passage to a Varian 4800 MicroGC, which measured non-condensable gases.

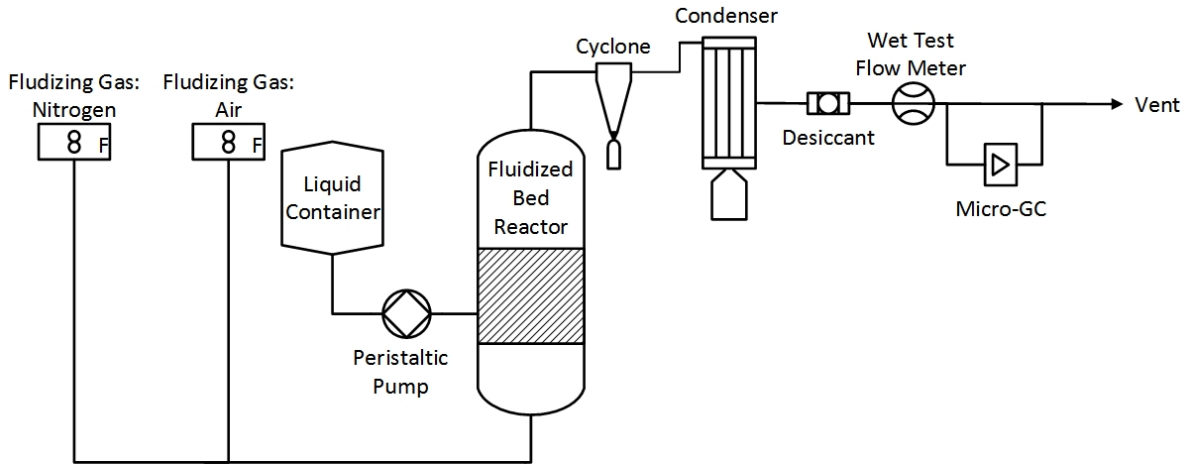

Figure 1. Reactor block flow diagram used for kinetic studies.

2.2. Calculation of levoglucosan decomposition rate coefficient from conversion data

For the levoglucosan decomposition experiments, a 20 wt. % solution of levoglucosan in water was continuously fed into the fluidized bed reactor at approximately 3.5 g min^{-1} using 3.5 SLPM of nitrogen as the inert fluidization gas. Gas residence time in the reactor was approximately one second. The transfer line was maintained at the reactor temperatures to avoid condensation of products ahead of the condenser, which rapidly cooled products to 10°C that were collected in a 250 ml bottle. Aerosols formed during this process were subsequently collected in glass wool. Experiments were of sixty minutes duration to ensure steady state was achieved.

Analysis of levoglucosan in the collected liquid product was accomplished with high performance liquid chromatography (HPLC), which is detailed elsewhere.[25] In addition to liquid product collected in the bottle, it was discovered a significant amount of levoglucosan aerosols were formed and trapped in the glass wool following the condenser. To analyze these collected

aerosols, 1.5 g of glass wool was placed into a 10 ml of water to dissolve the levoglucosan and other water-soluble compounds. After thorough mixing, 2 mL of the solution was extracted via a syringe and analyzed via GC-MS/FID. Quantification of the compounds was performed using the PolyARC system, with phenanthrene as an internal standard. As water droplets (aerosols) were also entrained in the gas stream, water was recovered in the glass wool packed bed. To account for this water mass, the remaining glass wool was dried at 105°C. The moisture content of the wool was calculated as the mass loss during the drying procedure. The dry mass of the glass wool, coupled with the GC-MS/FID analysis, was used to calculate the levoglucosan adsorbed on the filter.

Conversion of levoglucosan was calculated according to:

$$\mathbf{X} = {(\mathbf{M_F} - \mathbf{M_R})}/{\mathbf{M_F}} \quad (3)$$

where M_F is the mass of levoglucosan fed and M_R the mass of levoglucosan recovered. Identical to prior works, first order kinetics were assumed for the decomposition rate:

$$\mathbf{C_6H_{10}O_5} = (\mathbf{1} - \mathbf{X})\mathbf{C_6H_{10}O_5} + (\mathbf{X})\mathbf{C_aH_bO}_{\boldsymbol{d}} \quad (4)$$

$$\mathbf{r} = \mathbf{k}[\mathbf{C_6H_{10}O_5}]^{\mathbf{1}} \quad (5)$$

where $C_aH_bO_d$ are the grouped levoglucosan decomposition products, including non-condensable gases and various light oxygenated compounds. Two temperatures were used to calculate the gas phase decomposition at 500 and 550°C and compared to previous published works.

2.3. Calculation of global oxidation rates from oxygen conversion data

Three model compounds representing select pyrolysis products were employed in these oxidation experiments: levoglucosan, xylose, and acetic acid. They were prepared as an aqueous solution for continuous injection into the reactor by dissolving them in water. These concentrations were approximately 8wt. %, 20wt. % and 30wt. % solutions for xylose, levoglucosan, and acetic acid, respectively. The oxygen required for stoichiometric oxidation was adjusted based on the liquid feed rate for a specific model compound. The target equivalence ratio was 1.05 (excess oxygen) for all the experiments. With the air set at each condition for the target equivalence ratio, nitrogen was used as a balance to consistently flow 12 SLPM of gas for each experiment. The oxygen concentration in the sweep gas for the experiments was 3.0%, 7.7%, and 6.5-8.5% (experiment dependent) for the xylose, levoglucosan, and acetic acid experiments, respectively. The lower oxygen concentration for xylose was the result of the lower solution concentration, thus a larger percentage of the fluidizing gas was nitrogen as the sweep gas was kept constant at 12 SLPM. At a gas flow rate of 12 SLPM, the dynamic bed was expanded the entire fluid bed reactor height. Analysis of the non-condensable gases was accomplished with a MicroGC.

These experiments measured the conversion of oxygen between the inlet and outlet of the reactor rather than directly measure the conversion of the model compounds. Oxygen inlet concentration was calculated from the volumetric air flow rate entering the reactor while the exit concentration was directly measure with a MicroGC. This conversion of oxygen is written as follows:

$$\mathbf{X} = \left(\mathbf{O_2^{in}} - \mathbf{O_2^{out}}\right) \Big/ \mathbf{O_2^{in}} \quad (6)$$

where O_2^{in} is the inlet concentration of oxygen and O_2^{out} is the outlet concentration of oxygen. After a 20-minute stabilization period to achieve steady state, experimental data was collected

for 30 minutes. Given the combustion global model, the oxidation rate measures the rate of oxidation for the initial specie and its decomposition products. Thus, if the specie underwent rapid (i.e., instantaneous) decomposition, the global model would measure the rate of oxidation for those decomposition products. While multi-step models, or even more complex elementary mechanisms, can capture these competing decomposition versus oxidation reactions[14], deriving detailed reaction pathways is outside the scope for initial work.

Each model compound was oxidized at three different temperatures for the purpose of determining activation energies. Acetic acid and levoglucosan experiments were performed at set-point temperatures of 450, 500, and 550°C. The high reactivity of xylose forced operation at lower temperatures to avoid the complete conversion of oxygen, which would invalidate the measurements. However, the relatively low boiling point of xylose (415°C) set a lower bound on operating temperature to prevent its potential condensation in the transfer line. Accordingly, xylose was oxidized at 430, 465, and 500°C. The lower temperatures of the xylose experiments prevented its complete combustion in the fluidized bed reactor.

For these experiments, first order kinetics were assumed to oxygen, and zero order to the fuel. The order determination is a simplification; however, the low order (zero) in regard to the fuel source is consistent with previous works[22,23]:

$$\mathbf{C_aH_bO_d + \alpha O_2 = aCO_2 + \frac{b}{2}H_2O} \quad (7)$$

$$\mathbf{r = k(C_aH_bO_d)^0(O_2)^1} \quad (8)$$

where $C_aH_bO_d$ is the bio-oil specie, α the stoichiometric amount of oxygen required for combustion, r the oxidation rate, and k the kinetic rate coefficient (s^{-1}).

For each oxidation experiment, the temperature used to calculate rates was the average of the temperature measured by seven thermocouples in the fluidized bed. Notably, the internal temperature was often 10-15°C cooler than the set-point temperature of the reactor controller, which was based on the external wall temperature of the reactor. Determination of Arrhenius parameters is based on the internal reactor temperature.

2.4. Hydrodynamic model

For the purposes of analyzing the experimental results, the two-phase theory of fluidization was used to develop a hydrodynamic model of the reactor. The two-phase theory envisions a fluidized bed of consisting of an emulsion of sand and interstitial gas, and a bubble phase of discreet gas voids that rise through and interact with the emulsion phase. As shown in Figure 2, the emulsion phase can be modeled as a series of continuously stirred reactors (CSTR) while the bubble phase can be modeled as a series of plug flow reactors (PFR) in parallel with the train of CSTRs. Each pair of CSTR and PFR represents a stage of chemical reaction and is followed by an interaction module to account for heat and mass transfer between the two phases.[26] This idealization of hydrodynamics allows analytical solutions to be developed for simple chemical reactions in fluidized beds. The number of stages is commonly determined by an iterative process of matching modeling (two-phase theory) results with measured experimental data.[27] In this case, the number of stages was determined based on the growth of the bubble diameter, as subsequently described.

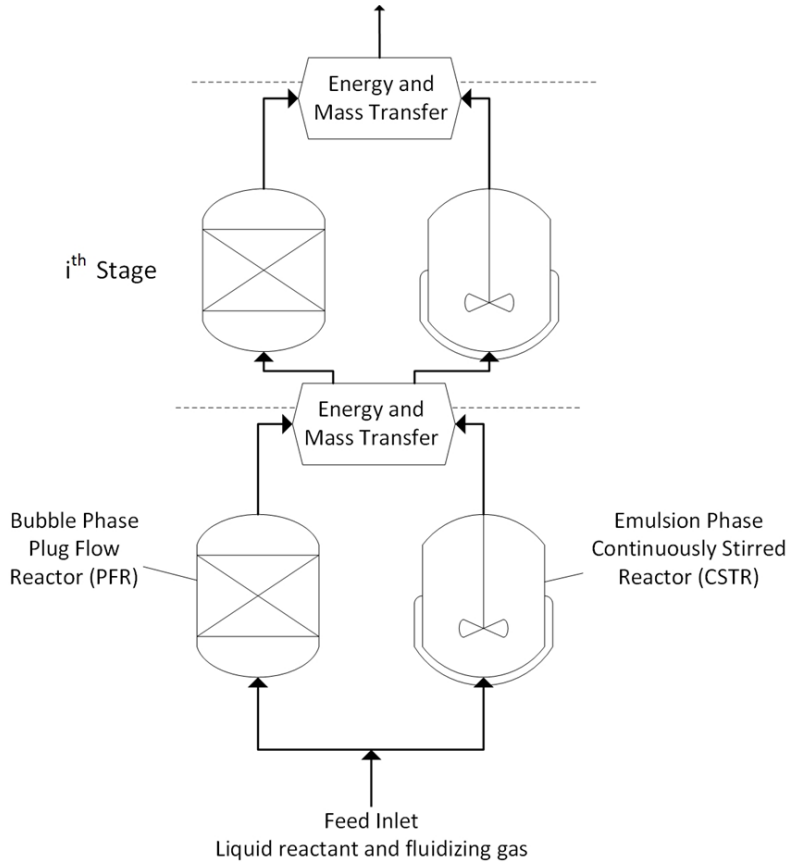

Figure 2. Two phase theory can be applied to model a fluidized bed reactor as a set of CSTRs and PFRs.

The conversion of reactant with first order kinetics in a plug flow reactor is given by [28]:

$$\mathbf{X_{PFR} = 1 - e^{(-k\tau_P)}} \quad (9)$$

where τ_P is the space time in the reactor, and k the kinetic rate coefficient.

The conversion of reactant in a CSTR with first order kinetics is given by:

$$\mathbf{X_{CSTR} = \frac{k\tau_C}{k\tau_C + 1}} \quad (10)$$

where τ_C is the space time in the reactor, and k the kinetic rate coefficient. At the end of each stage, the respective streams from the PFR and CSTR are mixed, with mass and energy transfer occurring. The overall conversion at the i^{th} stage exit is a function of the gas partition to the PFR and CSTR with their respective conversions:

$$\mathbf{X_R = \alpha X_{PFR} + (1 - \alpha) X_{CSTR}} \quad (11)$$

where X_R is the conversion at that stage, α the PFR gas partition coefficient, X_{PFR} the conversion that occurred in the reactor PFR, and X_{CSTR} the conversion of specie in the reactor CSTR. At this point, the reacted gas stream is repartitioned into the next CSTR and PFR (based on two-phase theory calculations), with the process repeated as necessary for each subsequent stage.

To calculate the gas apportioned to each the PFR and CSTR, several correlations from the literature were used to calculate the two-phase theory parameters (Table 3).[29,30]

The two-phase theory correlations (Table 3) were derived from experimental studies of fluidized beds. While several of the parameters are universally accepted (e.g., minimum fluidization velocity, Archimedes number), several methods for calculating bubble diameter have been proposed. Several studies[27,29,32] calculate bubble diameter according to Cai et al.[33]though the correlation of Mori and Wen[31] appears to be more appropriate for the small reactor employed in our study and has been successfully employed by other researchers to model fluidized processes.[34]

To determine α (the PFR gas partition coefficient), a series of calculations are required. First, the minimum fluidization velocity (U_{umf}) is calculated. Next, the initial bubble diameter at the bed inlet is calculated. The correlation was originally developed for a sintered plate serving as the distributor plate. To approach this behavior, several <100 μm sieve screens were placed over the distributor plate of the fluidized bed reactor used in experiments. The maximum bubble diameter is calculated as a function of the reactor diameter using a correlation

Table 3. Correlations used for two phase theory of fluidization calculations.

Parameter	Correlation	Ref
Archimedes Number	$Ar = \rho_g \times d_s^3 \frac{(\rho_s - \rho_g)g}{\mu_g^2}$	(35)
minimum fluidization velocity (U_{umf})	$U_{umf} = \frac{(\sqrt{27.2^2 + 0.0408Ar} - 27.2)\mu_g}{\rho_g \times d_{sand}}$	(35)
bubble diameter initial	$d_{b,i} = 0.00376(U_o - U_{umf})$	(31)
max diameter	$d_m = 0.652(A(U_o - U_{umf}))^{0.4}$	(31)
bubble size	$d_b = -[(exp\left(-0.3\left(\frac{H_r}{d_{Bed}}\right)\right)(d_m - d_{b,i})] + d_m$	(31)
velocity bubble	$U_b = U_O - U_{umf} + 0.711[(9.81d_b)^{0.5}]$	(36)
volume % PFR	$\alpha = \frac{U_o - U_{umf}}{U_b}$	(37)
Bubble to emulsion mass transfer	$\frac{1}{K} = \frac{1}{K_{ce}} + \frac{1}{K_{bc}}$	(38)
Mass Transfer: cloud to emulsion	$K_{ce} = 6.77\left(\frac{D_{AB}e_{mf}0.711(gd_b)^{0.5}}{d_b^3}\right)^{0.5}$	(39)
Mass Transfer: bubble to cloud	$K_{bc} = 4.5\left(\frac{U_{mf}}{d_b}\right) + 5.85\frac{D_{AB}^{0.5}g^{0.25}}{d_b^{1.25}}$	(39)

that assumes bubble coalescence into a single large bubble for very deep beds.[31] A separate correlation is used to calculate bubble size (diameter) as a function the vertical position in the bed because of bubble coalescence. The rise velocity of bubbles is a function of bed diameter at

each vertical position in the bed. The gas partitioned to the PFR is a function of bubble velocity with the remainder of the total gas flow partitioned to the emulsion (CSTR).

The mass transfer coefficient was calculated from the bubble diameter to the cloud (immediately surround the bubble) and then from the cloud to emulsion. The diffusion coefficient was calculated as ideal mixtures of naphthalene (surrogate for the combustion species[40]) in air or nitrogen for the oxidation and decomposition experiments, respectively. Given the relatively small bubble diameter (because of the narrow bed diameter of 0.0381m) the mass transfer coefficient was >10 s^{-1} for all conditions. Thus, the two exit concentrations from the PFR an CSTR are assumed to perfectly mix (equal concentration) at the conclusion of each stage. Likewise, heat transfer effects were assumed negligible, as the sweep gas and liquid solution kept both phases isothermal.

Shown in Figure 3 is the gas percentage calculated for the PFR versus reactor height, with the dashed line (at 0.05m) indicating the location of the liquid injection port.

To calculate τ_{RP} (PFR gas residence time) at each stage, the height of that stage is divided by the average gas bubble velocity:

$$\boldsymbol{\tau_{P,i}} = \frac{\boldsymbol{H_i}}{\boldsymbol{U_{b,i}}} \tag{12}$$

where H_i the height (distance) of that i^{th} stage of the PFR, and $U_{b,i}$ the average bubble velocity. The CSTR gas residence time is calculated as a function of the reactor volume (the balance not partitioned to the PFR) and the gas volumetric flow rate (the balance of the volumetric flow not partitioned to the PFR). The CSTR residence time is calculated using the following equations:

$$\mathbf{V_{C,i}} = \mathbf{H_i r^2 \pi (1 - \alpha)} \tag{13}$$

$$Q_{C,i} = Q_T(1 - \alpha) \quad (14)$$

$$\tau_{C,i} = \frac{V_{C,i}}{Q_{c,i}} \quad (15)$$

where r is the reactor radius (constant at 1.905 cm), H_i the height (distance) of that stage, $V_{C,i}$ the volume of CSTR at that stage fraction, Q_T the total (fluidizing gas and aqueous solution)

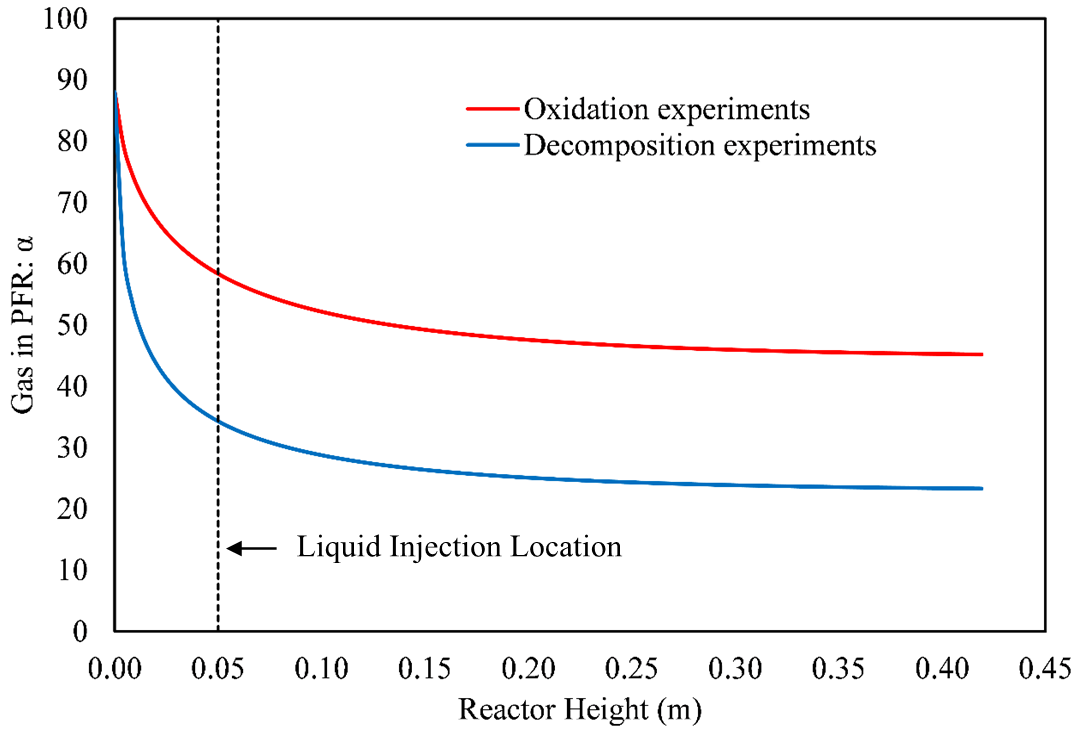

Figure 3. Gas percentage allocated to the PFR versus reactor height for typical operating conditions in oxidation and decomposition studies. The dashed line at 0.05m indicates location of liquid injection. For the decomposition experiments, the average sand particle size was 300 μm with a fluidizing gas flow rate of 3.5 SLPM of nitrogen. The oxidative experiments utilized 600 μm sand with 8 SLPM of nitrogen and 4 SLPM of air.

volumetric gas flow rate, $Q_{C,i}$ the CSTR volumetric gas flow rate, and $\tau_{C,i}$ the gas residence time for the CSTR in that fraction. This iterative process of determining the gas residence time was repeated for each stage fraction.

This analysis indicates that the fraction of gas partitioned to the PFR becomes almost constant at a height 0.15m above the distributor plate with a maximum bubble diameter attained. However, with gas partitioning still changing below a height of 0.15m, the reactor is split at this height of 0.15m, dividing the reactor into two stages to account for this difference in gas allocation. Additionally, to capture the reactions as the result of the back mixing of the specie and fluidizing gas below the liquid injection port, an additional CSTR (with no parallel PFR) is also implemented. Below 0.05m (liquid injection port) a CSTR captured any back mixing and the reactions that occurred below the liquid injection port. The subsequent gas allocated to the PFR in this stage is assumed to be unreacted, as the PFR does not allow for back mixing. Two in subsequent stages were used, with a divider at 0.15m, to model the fluid bed with different gas allocations for each stage. The reacted flow then entered the transfer line (modeled as a PFR) before the reactions were quenched in the condenser. This is represented in Figure 4.

At each stage, the reacted stream is repartitioned to the next CSTR and PFR. With the vapor stream now partially reacted, the conversion for the PFR reactor at the i^{th} stage for first order kinetics is now:

$$\mathbf{X_{PFR,i} = e^{-k\tau_{P,i}}(X_{i-1} + e^{k\tau_{P,i}} - 1)} \quad (16)$$

where τ_P is the space time in the reactor (at that stage), X_{i-1} the conversion from the previous stage, and k the kinetic rate coefficient as defined in Sections 2.2 and 2.3 This equation is also used to model the transfer line.

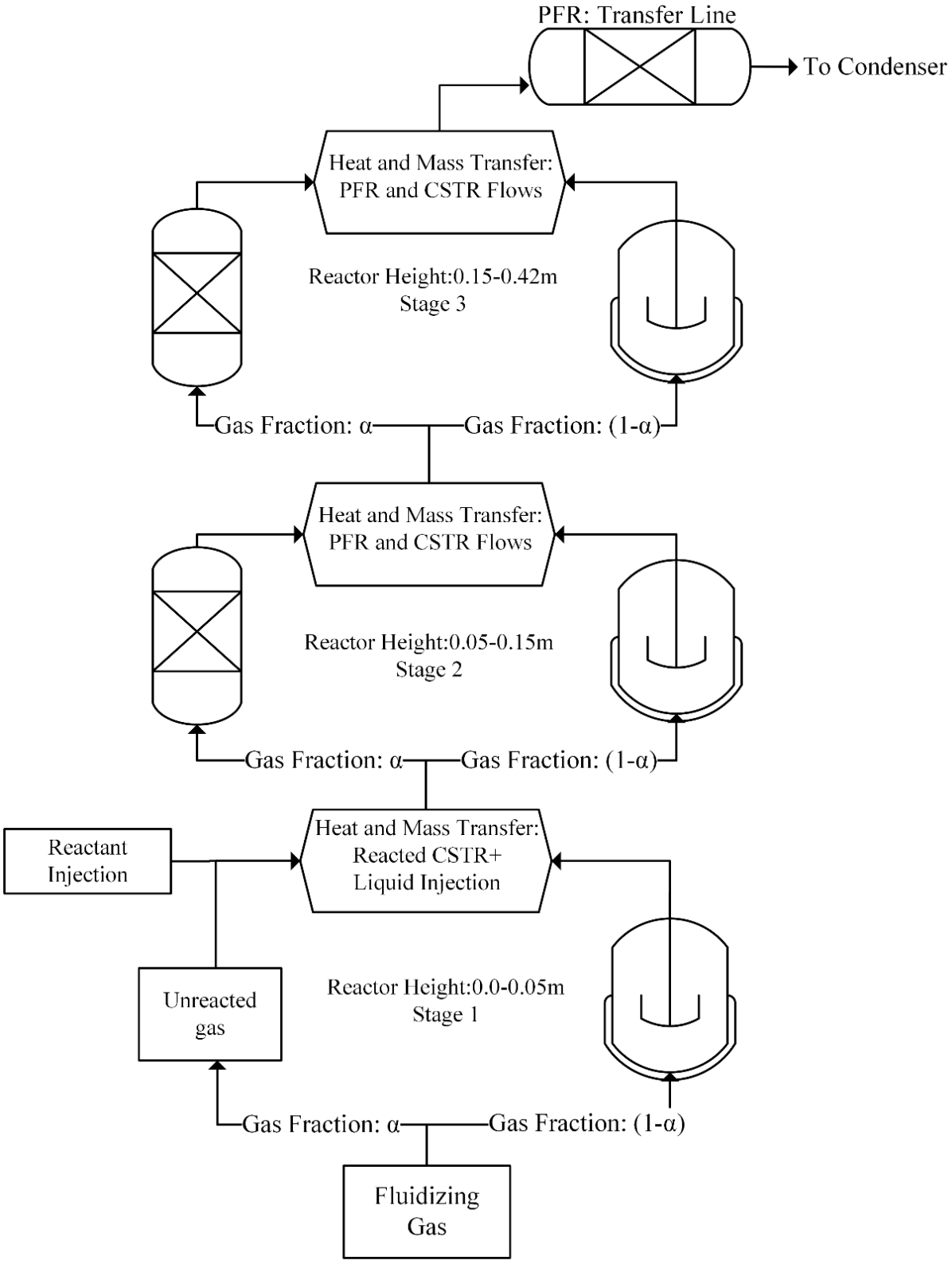

Figure 4. Two-phase theory calculations indicated three stages were necessary to model the bubbling fluid bed reactor. The first stage is just a CSTR with no PFR to account for back mixing of the liquid reactant and fluidizing gas.

Likewise, the CSTR conversion at the i^{th} stage for first order kinetics is written as following:

$$\mathbf{X_{CSTR,i}} = \frac{\mathbf{k\tau_{C,i} + X_{i-1}}}{\mathbf{k\tau_{C,i} + 1}} \quad (17)$$

where X_{i-1} is the conversion from the previous stage, and $\tau_{C,i}$ the gas residence time of the CSTR at that stage. By experimentally measuring X_T and calculating residence times and the gas partitioning coefficient from the two-phase theory, the kinetic rate coefficient can be solved numerically.

3. Results

3.1. Reactor repeatability

Triplicate trials were run for theacetic acid oxidation trials to determine experimental error. From the triplicate trials at a set-point temperature of 500°C, with internal temperature 489 ± 5°C, the average calculated kinetic rate coefficient of 0.20 s^{-1} had a standard sample deviation of ±0.02 s^{-1} with a confidence interval (95%) of ±0.04 s^{-1}. This excellent repeatability indicates single trials were sufficient to measure reaction kinetics. Consequently, all oxidation and decomposition experiments were single trials.

3.2. Levoglucosan decomposition measurement

For the experiments, the mass ratio of levoglucosan recovered to levoglucosan fed represented its conversion (as calculated using equation 3). As expected, the conversion was less at 500°C compared to 550°C. The decomposition conversion of levoglucosan at 550°C is similar to that of previous work[8], indicating the validity of this experimental method used in the present study. The total mass fed and mass recovered is reported in Table 4.

Table 4. Mass of levoglucosan fed during decomposition experiments.

Temperature (°C)	Levoglucosan Concentration (wt. %)	Total Solution Fed (g)	Mass Levoglucosan Fed (g)
500	23.7	164.0	38.9
550	23.7	203.4	48.2

Notably, for both trials a large fraction of levoglucosan (reported in Table 5) was recovered as aerosols in the glass wool. The recovery of levoglucosan aerosols has been reported in previous work, with collection accomplished using an electro-static precipitator (ESP).[41] Considering that the gas residence time was approximately one second, the relatively high conversion of levoglucosan indicates it is reactive to decomposition at pyrolysis temperatures. These results emphasize the importance of minimizing gas residence time to avoid unwanted decomposition of bio-oil vapors.[42]

Table 5. Levoglucosan decomposition was 50% greater at 550°C as compared to 500°C. The relatively high measured decomposition of levoglucosan indicates it is reactive to decomposition at pyrolysis temperatures.

Temperature (°C)	Mass Recovered Condenser (g)	Mass Recovered Glass Wool (g)	Total Levoglucosan Recovered (g)	Conversion[1]
500	12.6	13.6	26.3	0.32
550	16.7	8.6	25.3	0.48

[1] Calculated using Equation 3

3.3. Conversion for oxidation experiments

With an auto ignition temperature of 464°C[43], acetic acid oxidation was hypothesized to be minimal at the low end of typical pyrolysis temperatures. Virtually no information is available on low temperature oxidation of sugars. We hypothesized that the globaloxidation rates of sugars would be proportional to their decomposition rates in the absence of oxygen. Because the liquid phase decomposition of xylose is an order of magnitude greater than other sugars[44] and is

produced at low yields during pyrolysis compared to levoglucosan[45], we hypothesized that xylose would oxidize at greater rates than levoglucosan.

Table 6 gives oxygen conversion as calculated from oxygen inlet and outlet concentrations. The lower oxygen conversion for acetic acid indicates it is less reactive than the sugar species at these temperatures. Subsequent calculation of the kinetic rate coefficient quantifies these differences.

Table 6. Measured oxidation conversion for acetic acid, xylose, and levoglucosan oxidation trials. The consumption of oxygen in the reactive based on the change in concentration was used to calculate the oxidation conversion. Triplicate trials with acetic acid at a reactor temperature of ~490°C indicate excellent reactor repeatability.

Specie	Reactor Temperature (°C)	O_2 Inlet Concentration (v/v)	O_2 Outlet Concentration (v/v)	Conversion[1] (%)
Acetic Acid	438	8.75	8.22	6.0
	435	8.75	8.27	5.4
	489	8.75	7.88	10.0
	485	8.75	7.78	11.1
	495	6.48	5.68	12.3
	535	8.75	6.91	21.1
	540	8.75	5.76	34.2
Levoglucosan	435	7.70	6.29	18.3
	495	7.70	4.39	43.0
	550	7.70	3.22	58.1
Xylose	430	2.98	1.51	49.2
	465	2.98	1.38	53.5
	500	2.98	1.19	60.1

[1] Calculated from oxygen conversion using Equation 6.

3.4. Levoglucosan decomposition kinetic parameters

The global rate of levoglucosan conversion under inert conditions was measured at two (internal) reactor temperatures: 500 and 550°C. As shown in Table 7, the measured levoglucosan decomposition kinetic rate coefficient was 0.68 s^{-1} and 0.36 s^{-1} at 550 and 500°C, respectively similar to the values of 0.96 s^{-1} and 0.24 s^{-1} calculated by Fukutome et al.[8] Likewise, comparison

with whole bio-oil decomposition rates showed our values to be within the range of previous work.[10–12]

Table 7. Calculated two-phase decomposition rates using the two phase theory is similar previous works for bio-oil and levoglucosan.

			Levoglucosan Rate Coefficient (s^{-1})	
Source	Activation Energy (kJ mol^{-1})	Pre-Exponential Factor (s^{-1})	500°C	550°C
This work	66.0	1.05×10^{4}	0.36	0.68
Fukutome et al. [8]	147.2	2.03×10^{9}	0.24	0.96
			Bio-oil Rate Coefficient (s^{-1})	
Liden et al. [10]	76.6	4.00×10^{4}	0.23	0.55
Morf et al. [11]	107.5	4.28×10^{6}	0.27	0.64
Baumlin et al.[12]	59.0	1.93×10^{3}	0.20	0.35

From these measured decomposition rate coefficients, the activation energy and pre-exponential factor was calculated as 66.0 kJ mol^{-1} and 10500 s^{-1}, respectively. While this activation energy is lower than the work of Fukutome et al.[8] (147 kJ mol^{-1}), it is in the range of the global decomposition models of 59-107 kJ mol^{-1}.[10–12] The agreement between our work and the previous work of Fukutome using different analytical methods validates our use of the two-phase theory of fluidization to represent the hydrodynamics of our reactor system.

3.5. Arrhenius parameters for global oxidation rates

Oxygen conversion during the oxidation experiments with acetic acid, levoglucosan, and xylose was used to calculate the kinetic rate coefficients as functions of temperature and plotted on an Arrhenius plot (Figure 5). Favorably, the global oxidation rate coefficient measured by Smoot and Smith [22] at 500°C (0.58 s^{-1}) falls in the range of the rate coefficients measured in our study (0.29-2.03 s^{-1}), which serves as a validation of our methodology. In contrast, the global combustion model of Dryer and Westbrook[23] overestimates the oxidation rate by at least of

factor of 10 (50.44 s^{-1} at 500°C). We think this poor match arises from Dryer and Westbrook's measurements at temperatures more typical of complete combustion (>800°C).

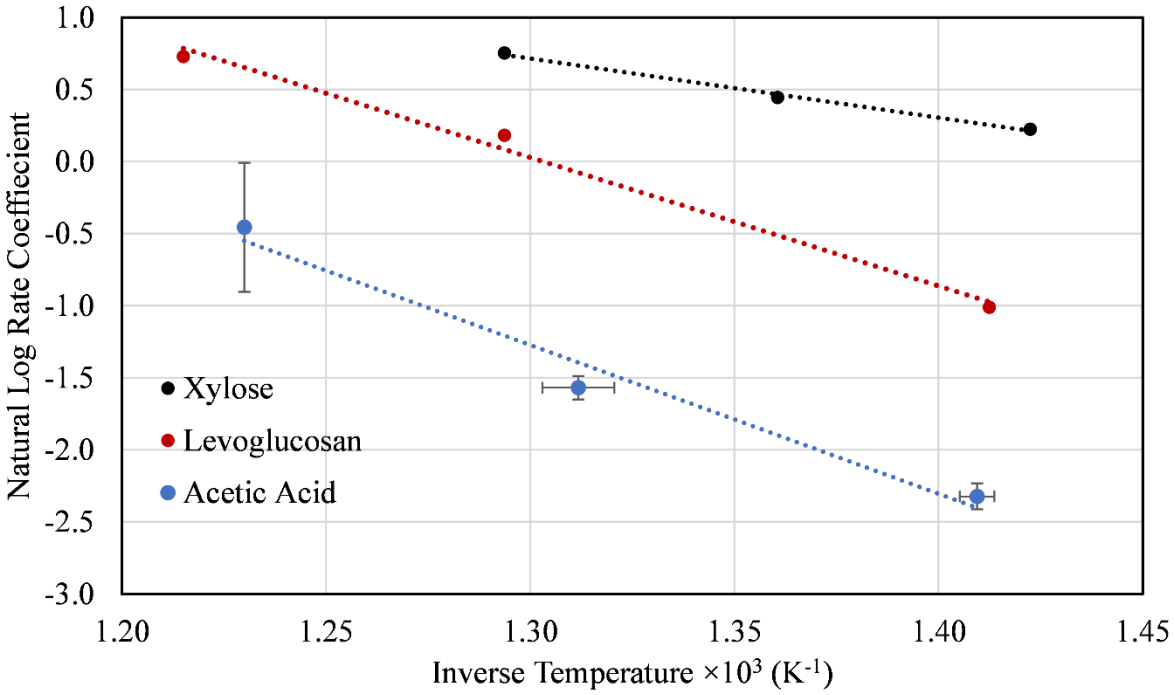

Figure 5. Arrhenius plot of the global oxidation rates of the three-ideal bio-oil components. Error bars on the acetic acid trials are the sample standard deviation from replicate trials and the average internal temperature for each trial. Note: levoglucosan and xylose only had single trials performed.

Levoglucosan and xylose were much more reactive than acetic acid. At pyrolysis temperatures, levoglucosan oxidized at a rate several fold higher than for acetic acid. We hypothesize that the greater global oxidation rate of levoglucosan compared to acetic acid is the result of its greater propensity to decompose into reactive products, which is enhance in the presence of oxygen. Previous studies have found molecular oxygen to be a decomposition accelerant, acting as a radical initiator for cracking (decomposition) reactions.[46] Notably, at identical conditions (e.g., temperature, pressure, gas residence time), introduction of a small amount of oxygen is known to increase by thirty-fold the conversion rate of hexane to lighter alkenes. The similar yields of

these decomposition products attained indicates that the conversion is not simply the result of direct oxidation.[47] Similarly, in the presence of oxygen, levoglucosan is likely to undergo both oxidation and accelerated decomposition to light oxygenates, which are themselves susceptible to oxidation. For example, acetaldehyde, among the most prominent of these light oxygenates,[8] readily oxidizes at temperatures below 400°C. This mechanism of oxygen-catalyzed decomposition of levoglucosan and oxidation of the decomposed products could explain the faster oxidation kinetic rate of levoglucosan as compared to acetic acid. The proposed reaction scheme, decomposition followed by oxidation, is a simplification of traditional oxidation pathways. Typically, combustion studies detail the decomposition and oxidation of the specie, determining radical and stable intermediate species through (typically) hundreds of pathways and reactions.[48] These mechanisms conclude that oxygenated radicals are responsible for the decomposition of the initial combustion specie (in effect oxygen catalyzed decomposition) starting the oxidation process. Thus, while these mechanisms involve more detail, our simplification of oxidative decomposition with subsequent oxidation is consistent with combustion studies. Consequently, the greater reactivity of levoglucosan's decomposition products offers an explanation to its greater reactivity as compared to acetic acid.

In contrast, acetic acid is stable against decomposition at temperatures up to 700°C.[49] Its decomposition products are methane and carbon monoxide, both of which have autoignition temperatures higher than typical pyrolysis temperatures.[50] Accordingly, it is not surprising that acetic acid does not readily oxidize compared to levoglucosan and xylose.

The calculated activation energy for acetic acid and levoglucosan was measured to be 84.4 ± 12.0 kJ mol^{-1} and 74.0 kJ mol^{-1}, respectively. Favorably, the two values are similar and within

the uncertainty of each other, though their oxidation reactivity at pyrolysis temperatures vary by a factor of at least three.

In contrast, xylose had an activation energy of only 34.1 kJ mol^{-1}, substantially lower than measured for acetic acid and levoglucosan. Conversely, it was also the most reactive specie of the three. While the greater oxidative reactivity was expected due to its instability[44], the low apparent activation energy indicates an oversight with the global model. A hypothesis for this low activation energy is discussed. All three activation energies can be found in Table 8.

Table 8. Arrhenius parameters of the three global oxidation models. Sample standard deviation for acetic acid activation energy is indicated with the plus and minus sign. Comparison with previous global oxidation models indicate that the measured rate coefficients were comparable at pyrolysis temperatures. Notably, the Smoot and Smith[22] rate coefficient is a modified Arrhenius equation with a temperature exponential of 0.3.

			Calculated Kinetic Rate Coefficient (s^{-1})		
Specie	**Activation Energy (kJ mol^{-1})**	**Pre-Exponential Factor (s^{-1})**	**400°C**	**500°C**	**600°C**
Acetic Acid	84.4 ± 12.0	1.44×10^{5}	0.04	0.29	1.28
Levoglucosan	74.0	1.06×10^{5}	0.19	1.06	3.96
Xylose	34.1	4.07×10^{2}	0.92	2.03	3.73
Smoot and Smith [22]	80.2	2.07×10^{2}	0.09	0.58	2.51

Xylan pyrolysis and xylose decomposition produce several light oxygenates (e.g., acetic acid and acetol), as well various furan/pyranose ring derivatives.[45,51] These products are formed through a combination of xylose dehydration and ring fragmentation, which appear to have similar activation energies and rates of formation.[52,53] Given the apparent instability of xylose, it is hypothesized decomposition rapidly occurs at these conditions producing these various light oxygenated compounds which are subject to oxidation. In particular, the inert decomposition kinetic rate coefficient of xylose to light oxygenates and gases at 433°C was measured to be 72.7 s^{-1}, which is orders of magnitude higher than the decomposition rate of levoglucosan. While this rate appears quite fast, it is consistent with liquid phase decomposition rates demonstrating the

instability of xylose.[44] Concluding that xylose is rapidly decomposing, two of the most prominent decomposition products from xylose are furfural and formic acid.[44] However, these decomposition products have markedly different autoignition temperatures of 315°C and 520°C for furfural and formic acid, respectively. This markable difference in reactivity and the conditions used to measure the global oxidation rate is likely responsible for the lower apparent activation energy.

Shown in Figure 6, is a simplified reaction mechanism of xylose decomposing to two compounds: formic acid and furfural. The rate of decomposition (k_{d1} and k_{d2}) is assumed sufficiently fast that it occurs immediately in the reactor and at equal rates (in effect producing an equal concentration of the two species) before oxidation occurred to xylose. Then, oxidation occurs to formic acid (k_{O1}) and furfural (k_{O2}) with separate global oxidation rates for each, assuming formic acid has a low oxidative reactivity, and furfural has faster/greater oxidative reactivity.

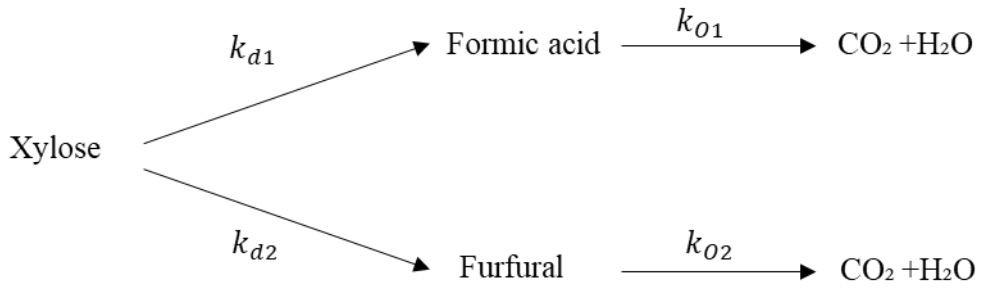

Figure 6. Simplified reaction pathway for xylose decomposition and oxidation. The decomposition rates are presented as k_{d1} and k_{d2} while the oxidation reaction rates are k_{O2} and k_{O1}. Note: the pathways are hypothetical and accordingly are not balanced molar equations.

This duality of one specie rapidly oxidizing within the space time (residence time) of the reactor and the other specie oxidizing at a slower rate would result in a low apparent activation energy. To demonstrate this effect, a single PFR was used to model the fluidized bed reactor with a gas

residence time of 0.75 seconds. In this model, it is assumed that xylose immediately decomposes to furfural and formic acid (as depicted in Figure 6) at an equal fraction, which are then subject to oxidation. The simplified model has two global oxidation rates, with equal activation energies for k_{O1} and k_{O2} at 84.4 kJ mol^{-1} (the measured apparent activation energy of acetic acid), though have different pre-exponential factors of 1.44×10^5 (as measured for acetic acid) and 3.60×10^6 for the low (k_{O1}-formic acid) and high (k_{O2}-furfural) reactivity, respectively. The pre-exponential factor and the calculated oxidation kinetic rate coefficient for furfural is an estimate, however the greater reactivity is assumed based on its low autoignition temperature.

Calculating the oxygen conversion for each pathway (assuming a 50/50 split of oxygen for each pathway), if one specie (or several) rapidly consumes oxygen and has complete conversion, while the other has a slower global oxidation rate, a low apparent activation energy for overall oxidation of the specie is calculated. This is demonstrated in Table 9, as the highly reactive species has complete oxidative conversion (under these conditions) while the lowly reactive specie has incomplete conversion. Consequently, the use of a global model may not accurately capture these conflicting parallel reactions, resulting in a low activation energy. For the example provided, the activation energy is equal to ~35 kJ mol^{-1}. While the global oxidation model utilized may not accurately capture the reaction pathway for xylose, the measured global oxidation rate is still valuable.

Table 9. Rapid decomposition of xylose with subsequent oxidation of the decomposed products could result in a low measured apparent oxidation activation energy if their oxidative reactivity were significantly different. Note: these are theoretical rates and do not reflect experimental conditions.

	Model oxygen conversion (%)		
Temperature (°C)	High oxidative reactivity (furfural)	Low oxidative reactivity (formic acid)	Total (%)
430	38.2	2.8	41.0
465	47.2	5.4	52.6

500	49.8	9.6	59.4

Future work would focus on determining the oxidation reactivity of these xylose decomposition products (e.g., furfural, formic acid), to support this low measured apparent activation energy. Nevertheless, the global oxidation rates of these three species are the first of their kind, providing valuable kinetic data supporting modeling efforts of autothermal pyrolysis.

4. Conclusions

This study investigated global oxidation rates of prominent products of fast pyrolysis of lignocellulosic biomass at temperatures appropriate to autothermal pyrolysis. Experiments were performed in a fluidized bed reactor. Hydrodynamics of the reactor were modeled with the two-phase theory of fluidization and validated by comparing decomposition rates for levoglucosan with results from previous researchers. Global oxidation rates for levoglucosan, xylose, and acetic acid at 500°C varied by an order of magnitude (0.29-2.03 s^{-1}). To the authors knowledge, the global oxidation rates derived are the first of their kind for bio-oil products relevant to autothermal pyrolysis. These results will be useful in efforts to develop reaction models of autothermal pyrolyzers.

5. Acknowledgements

This paper is based upon work supported by the Department of Energy under Award Number EE0008326 and DE-AC36-08GO28308. It was prepared as an account of work sponsored by an agency of the United States Government. Neither the United States Government nor any agency thereof, nor any of their employees, makes any warranty, express or implied, or assumes any legal liability or responsibility for the accuracy, completeness, or usefulness of any information,

apparatus, product, or process disclosed, or represents that its use would not infringe privately owned rights. Reference herein to any specific commercial product, process, or service by trade name, trademark, manufacturer, or otherwise does not necessarily constitute or imply its endorsement, recommendation, or favoring by the United States Government or any agency thereof. The views and opinions of authors expressed herein do not necessarily state or reflect those of the United States Government or any agency thereof.

Nomenclature:

Parameters:
A=cross-sectional area reactor (m^2)
Ar=Archimedes number
$d_{b,i}$=Initial bubble diameter (m)
d_m=Maximum bubble diameter (m)
d_s=diameter sand (m)
d_b=bubble diameter (m)
g=gravitational acceleration ($m\ s^{-2}$)
H_{rec}=Reactor height (m)
U_b=velocity of bubble ($m\ s^{-1}$)
U_o=Superficial gas velocity ($m\ s^{-1}$)
U_{umf}=minimum fluidization velocity ($m\ s^{-1}$)
α=Gas percentage in bubble phase

Greek:
ρ_g=density of fluidizing gas ($kg\ m^{-3}$)
ρ_s=density of sand
μ_g= dynamic viscosity gas, ($kg\ m^{-1}s^{-1}$)

Super and Sub Scripts:
b=bubble
i=initial or stage
g=gas
r=reactor

References:

(1) Bridgwater, A. V.; Meier, D.; Radlein, D. An Overview of Fast Pyrolysis of Biomass.

Org. Geochem. **1999**, *30* (12), 1479–1493. https://doi.org/10.1016/S0146-6380(99)00120-5.

(2) Brown, R. C. Process Intensification through Directly Coupled Autothermal Operation of Chemical Reactors. *Joule* **2020**, *4* (11), 2268–2289. https://doi.org/10.1016/j.joule.2020.09.006.

(3) Polin, J. P.; Peterson, C. A.; Whitmer, L. E.; Smith, R. G.; Brown, R. C. Process Intensification of Biomass Fast Pyrolysis through Autothermal Operation of a Fluidized Bed Reactor. *Appl. Energy* **2019**, *249*, 276–285. https://doi.org/10.1016/J.APENERGY.2019.04.154.

(4) Polin, J. P.; Carr, H. D.; Whitmer, L. E.; Smith, R. G.; Brown, R. C. Conventional and Autothermal Pyrolysis of Corn Stover: Overcoming the Processing Challenges of High-Ash Agricultural Residues. *J. Anal. Appl. Pyrolysis* **2019**, *143* (July), 104679. https://doi.org/10.1016/j.jaap.2019.104679.

(5) Tsang, W.; Hampson, R. F. Chemical Kinetic Data Base for Combustion Chemistry. Part I. Methane and Related Compounds. *J. Phys. Chem. Ref. Data* **1986**, *15* (3), 1087–1279. https://doi.org/10.1063/1.555759.

(6) Marinov, N. M. A Detailed Chemical Kinetic Model for High Temperature Ethanol Oxidation. *Int. J. Chem. Kinet.* **1999**, *31* (3), 183–220. https://doi.org/10.1002/(SICI)1097-4601(1999)31:3<183::AID-KIN3>3.0.CO;2-X.

(7) Peterson, C. A.; Brown, R. C. Oxidation Kinetics of Biochar from Woody and Herbaceous Biomass. *Chem. Eng. J.* **2020**, *401* (June), 126043.

https://doi.org/10.1016/j.cej.2020.126043.

(8) Fukutome, A.; Kawamoto, H.; Saka, S. Kinetics and Molecular Mechanisms for the Gas-Phase Degradation of Levoglucosan as a Cellulose Gasification Intermediate. *J. Anal. Appl. Pyrolysis* **2017**, *124*, 666–676. https://doi.org/10.1016/J.JAAP.2016.12.010.

(9) Shin, E.-J.; Nimlos, M. R.; Evans, R. J. Kinetic Analysis of the Gas-Phase Pyrolysis of Carbohydrates. *Fuel* **2001**, *80* (12), 1697–1709. https://doi.org/10.1016/S0016-2361(01)00056-4.

(10) Liden, A. G.; Berruti, F.; Scott, D. S. A Kinetic Model for the Production of Liquids from the Flash Pyrolysis of Biomass. *Chem. Eng. Commun.* **1988**, *65* (1), 207–221. https://doi.org/10.1080/00986448808940254.

(11) Morf, P.; Hasler, P.; Nussbaumer, T. Mechanisms and Kinetics of Homogeneous Secondary Reactions of Tar from Continuous Pyrolysis of Wood Chips. *Fuel* **2002**, *81* (7), 843–853. https://doi.org/10.1016/S0016-2361(01)00216-2.

(12) Baumlin, S.; Broust, F.; Ferrer, M.; Meunier, N.; Marty, E.; Lédé, J. The Continuous Self Stirred Tank Reactor: Measurement of the Cracking Kinetics of Biomass Pyrolysis Vapours. *Chem. Eng. Sci.* **2005**, *60* (1), 41–55. https://doi.org/10.1016/j.ces.2004.07.057.

(13) Lindstrom, J. K.; Proano-Aviles, J.; Johnston, P. A.; Peterson, C. A.; Stansell, J. S.; Brown, R. C. Competing Reactions Limit Levoglucosan Yield during Fast Pyrolysis of Cellulose. *Green Chem.* **2019**, *21* (1), 178–186. https://doi.org/10.1039/C8GC03461C.

(14) Frassoldati, A.; Cuoci, A.; Faravelli, T.; Niemann, U.; Ranzi, E.; Seiser, R.; Seshadri, K. An Experimental and Kinetic Modeling Study of N-Propanol and Iso-Propanol

Combustion. *Combust. Flame* **2010**, *157* (1), 2–16. https://doi.org/10.1016/j.combustflame.2009.09.002.

(15) Debiagi, P. E. A.; Gentile, G.; Pelucchi, M.; Frassoldati, A.; Cuoci, A.; Faravelli, T.; Ranzi, E. Detailed Kinetic Mechanism of Gas-Phase Reactions of Volatiles Released from Biomass Pyrolysis. *Biomass and Bioenergy* **2016**, *93*, 60–71. https://doi.org/10.1016/j.biombioe.2016.06.015.

(16) Ranzi, E.; Debiagi, P. E. A.; Frassoldati, A. Mathematical Modeling of Fast Biomass Pyrolysis and Bio-Oil Formation. Note II: Secondary Gas-Phase Reactions and Bio-Oil Formation. *ACS Sustain. Chem. Eng.* **2017**, *5* (4), 2882–2896. https://doi.org/10.1021/acssuschemeng.6b03098.

(17) Ranzi, E.; Frassoldati, A.; Stagni, A.; Pelucchi, M.; Cuoci, A.; Faravelli, T. Reduced Kinetic Schemes of Complex Reaction Systems: Fossil and Biomass-Derived Transportation Fuels. *Int. J. Chem. Kinet.* **2014**, *46* (9), 512–542. https://doi.org/10.1002/kin.20867.

(18) Ranzi, E.; Cavallotti, C.; Cuoci, A.; Frassoldati, A.; Pelucchi, M.; Faravelli, T. New Reaction Classes in the Kinetic Modeling of Low Temperature Oxidation of N-Alkanes. *Combust. Flame* **2015**, *162* (5), 1679–1691. https://doi.org/10.1016/J.COMBUSTFLAME.2014.11.030.

(19) Dhahak, A.; Bounaceur, R.; Le Dreff-Lorimier, C.; Schmidt, G.; Trouve, G.; Battin-Leclerc, F. Development of a Detailed Kinetic Model for the Combustion of Biomass. *Fuel* **2019**, *242*, 756–774. https://doi.org/10.1016/J.FUEL.2019.01.093.

(20) Lu, H.; Robert, W.; Peirce, G.; Ripa, B.; Baxter, L. L. Comprehensive Study of Biomass Particle Combustion. *Energy and Fuels* **2008**, *22* (4), 2826–2839. https://doi.org/10.1021/ef800006z.

(21) Johansson, R.; Thunman, H.; Leckner, B. Influence of Intraparticle Gradients in Modeling of Fixed Bed Combustion. *Combust. Flame* **2007**, *149* (1–2), 49–62. https://doi.org/10.1016/j.combustflame.2006.12.009.

(22) Smoot, L. D.; Smith, P. J. *Coal Combustion and Gasification*; Luss, D., Ed.; Springer US: Boston, MA, 1985. https://doi.org/10.1007/978-1-4757-9721-3.

(23) Dryer, F. L.; Westbrook, C. K. Simplified Reaction Mechanisms for the Oxidation of Hydrocarbon Fuels in Flames. *Combust. Sci. Technol.* **1981**, *27* (1–2), 31–43. https://doi.org/10.1080/00102208108946970.

(24) Dubey, R.; Bhadraiah, K.; Raghavan, V. On the Estimation and Validation of Global Single-Step Kinetics Parameters of Ethanol-Air Oxidation Using Diffusion Flame Extinction Data. *Combust. Sci. Technol.* **2011**, *183* (1), 43–50. https://doi.org/10.1080/00102202.2010.497516.

(25) Johnston, P. A.; Brown, R. C. Quantitation of Sugar Content in Pyrolysis Liquids after Acid Hydrolysis Using High-Performance Liquid Chromatography without Neutralization. *J. Agric. Food Chem.* **2014**, *62* (32), 8129–8133. https://doi.org/10.1021/jf502250n.

(26) Grace, J. R.; Clift, R. On the Two-Phase Theory of Fluidization. *Chem. Eng. Sci.* **1974**, *29* (2), 327–334. https://doi.org/10.1016/0009-2509(74)80039-4.

(27) Yousefifar, A.; Sotudeh-Gharebagh, R.; Mostoufi, N.; Mohtasebi, S. S. Sequential Modeling of Heavy Liquid Fuel Combustion in a Fluidized Bed. *Chem. Eng. Technol.* **2015**, *38* (10), 1853–1864. https://doi.org/10.1002/ceat.201400464.

(28) Scott Fogler, H. *Elements of Chemical Reaction Engineering*; Third edition. Upper Saddle River, N.J. : Prentice Hall PTR, [1999] ©1999, 2016.

(29) Eslami, A.; Hashemi Sohi, A.; Sheikhi, A.; Sotudeh-Gharebagh, R. Sequential Modeling of Coal Volatile Combustion in Fluidized Bed Reactors. *Energy and Fuels* **2012**, *26* (8), 5199–5209. https://doi.org/10.1021/ef300710j.

(30) Kopyscinski, J.; Schildhauer, T. J.; Biollaz, S. M. A. Fluidized-Bed Methanation: Interaction between Kinetics and Mass Transfer. *Ind. Eng. Chem. Res.* **2011**, *50* (5), 2781–2790. https://doi.org/10.1021/ie100629k.

(31) Mori, S.; Wen, C. Y. Estimation of Bubble Diameter in Gaseous Fluidized Beds. *AIChE J.* **1975**, *21* (1), 109–115. https://doi.org/10.1002/aic.690210114.

(32) Hashemi Sohi, A.; Eslami, A.; Sheikhi, A.; Sotudeh-Gharebagh, R. Sequential-Based Process Modeling of Natural Gas Combustion in a Fluidized Bed Reactor. *Energy and Fuels* **2012**, *26* (4), 2058–2067. https://doi.org/10.1021/ef300204j.

(33) Cai, P.; Schiavetti, M.; De Michele, G.; Grazzini, G. C.; Miccio, M. Quantitative Estimation of Bubble Size in PFBC. *Powder Technol.* **1994**, *80* (2), 99–109. https://doi.org/10.1016/0032-5910(94)02834-6.

(34) Yan, L.; Jim Lim, C.; Yue, G.; He, B.; Grace, J. R. One-Dimensional Modeling of a Dual Fluidized Bed for Biomass Steam Gasification. *Energy Convers. Manag.* **2016**, *127*, 612–

622. https://doi.org/10.1016/J.ENCONMAN.2016.09.027.

(35) Wen, C. Y.; Yu, Y. H. A Generalized Method for Predicting the Minimum Fluidization Velocity. *AIChE J.* **1966**, *12* (3), 610–612. https://doi.org/10.1002/aic.690120343.

(36) Darton, R.; LaNauze, R.; Davidson, J.; Harrison, D. Bubble Growth Due to Coalescence in Fluidised Beds. *Transcr. Inst. Chem. Eng.* **1977**, *55* (October 1977), 274–280.

(37) Kunii, D.; Levenspiel, O. *Fluidization Engineering*, 2nd ed.; Elsevier, 1991. https://doi.org/10.1016/C2009-0-24190-0.

(38) Kunii, D.; Levenspiel, O. Particle-to-Gas Mass and Heat Transfer. In *Fluidization Engineering*; Kunii, D., Levenspiel, O. B. T.-F. E. (Second E., Eds.; Elsevier: Boston, 1991; pp 257–276. https://doi.org/10.1016/B978-0-08-050664-7.50017-2.

(39) Kunii, D.; Levenspiel, O. Particle-to-Gas Mass and Heat Transfer. In *Fluidization Engineering*; Kunii, D., Levenspiel, O. B. T.-F. E. (Second E., Eds.; Elsevier: Boston, 1991; pp 257–276. https://doi.org/10.1016/B978-0-08-050664-7.50017-2.

(40) Proano-Aviles, J.; Lindstrom, J. K.; Johnston, P. A.; Brown, R. C. Heat and Mass Transfer Effects in a Furnace-Based Micropyrolyzer. *Energy Technol.* **2017**, *5* (1), 189–195. https://doi.org/10.1002/ente.201600279.

(41) Rover, M. R.; Johnston, P. A.; Whitmer, L. E.; Smith, R. G.; Brown, R. C. The Effect of Pyrolysis Temperature on Recovery of Bio-Oil as Distinctive Stage Fractions. *J. Anal. Appl. Pyrolysis* **2014**, *105*, 262–268. https://doi.org/10.1016/j.jaap.2013.11.012.

(42) Venderbosch, R. H. Fast Pyrolysis. In *Thermochemical Processing of Biomass*; Wiley Online Books; John Wiley & Sons, Ltd: Chichester, UK, 2019; pp 175–206.

https://doi.org/10.1002/9781119417637.ch6.

(43) Nicholas P. Setchkin. Self-Ignition Temperatures of Combustible Liquids. *J. Res. Natl. Bur. Stand. (1934).* **1954**, *53* (1), 49–66.

(44) Buera, M. del P.; Chirife, J.; Resnik, S. L.; Lozano, R. D. Nonenzymatic Browning in Liquid Model Systems of High Water Activity: Kinetics of Color Changes Due to Caramelization of Various Single Sugars. *J. Food Sci.* **1987**, *52* (4), 1059–1062. https://doi.org/10.1111/j.1365-2621.1987.tb14275.x.

(45) Patwardhan, P. R.; Brown, R. C.; Shanks, B. H. Product Distribution from the Fast Pyrolysis of Hemicellulose. *ChemSusChem* **2011**, *4* (5), 636–643. https://doi.org/10.1002/cssc.201000425.

(46) Peterson, J. D.; Vyazovkin, S.; Wight, C. A. Kinetics of the Thermal and Thermo-Oxidative Degradation of Polystyrene, Polyethylene and Poly(Propylene). *Macromol. Chem. Phys.* **2001**, *202* (6), 775–784. https://doi.org/10.1002/1521-3935(20010301)202:6<775::AID-MACP775>3.0.CO;2-G.

(47) Liu, X.; Li, W.; Xu, H.; Chen, Y. Production of Light Alkenes with Low CO2emission from Gas Phase Oxidative Cracking (GOC) of Hexane. *React. Kinet. Catal. Lett.* **2004**, *81* (2), 203–209. https://doi.org/10.1023/B:REAC.0000019424.06619.28.

(48) Jin, Z. H.; Yu, D.; Liu, Y. X.; Tian, Z. Y.; Richter, S.; Braun-Unkhoff, M.; Naumann, C.; Yang, J. Z. An Experimental Investigation of Furfural Oxidation and the Development of a Comprehensive Combustion Model. *Combust. Flame* **2021**, *226*, 200–210. https://doi.org/10.1016/j.combustflame.2020.12.015.

(49) Nguyen, M. T.; Sengupta, D.; Raspoet, G.; Vanquickenborne, L. G. Theoretical Study of the Thermal Decomposition of Acetic Acid: Decarboxylation Versus Dehydration. *J. Phys. Chem* **1995**, *99*, 11883–11888.

(50) Robinson, C.; Smith, D. B. The Auto-Ignition Temperature of Methane. *J. Hazard. Mater. Elsevier Sci. Publ. B.V* **1984**, *8*, 199–203.

(51) Gao, Z.; Li, N.; Wang, Y.; Niu, W.; Yi, W. Pyrolysis Behavior of Xylan-Based Hemicellulose in a Fixed Bed Reactor. *J. Anal. Appl. Pyrolysis* **2020**, *146* (August 2019), 104772. https://doi.org/10.1016/j.jaap.2020.104772.

(52) Wang, M.; Liu, C.; Li, Q.; Xu, X. Theoretical Insight into the Conversion of Xylose to Furfural in the Gas Phase and Water. *J. Mol. Model.* **2015**, *21* (11). https://doi.org/10.1007/s00894-015-2843-6.

(53) Huang, J.; He, C.; Wu, L.; Tong, H. Thermal Degradation Reaction Mechanism of Xylose: A DFT Study. *Chem. Phys. Lett.* **2016**, *658*, 114–124. https://doi.org/10.1016/j.cplett.2016.06.025.

Table of Contents Graphic